THE ASTROPHYSICAL JOURNAL, 460:949–963, 1996 April 1

EUVE SPECTROSCOPY OF β CANIS MAJORIS (B1 II–III) FROM 500 Å TO 700 Å

J. P. CASSINELLI,[1] D. H. COHEN,[1] J. J. MACFARLANE,[1,2] J. E. DREW,[3,4] A. E. LYNAS-GRAY,[3] I. HUBENY,[5] J. V. VALLERGA,[6] B. Y. WELSH,[7] AND M. G. HOARE[8]

Received 1995 June 19; accepted 1995 October 6

ABSTRACT

Observations of the bright variable star β CMa (B1 II–III) made with the *Extreme Ultraviolet Explorer* (*EUVE*) are presented. We report on the continuous energy distribution, photospheric line identification, and the variability of the star, as well as the physical implications for the structure of the local interstellar medium. The star is one of the strongest EUV sources in the long-wavelength spectrometer of *EUVE*, and one of only two early-type stars whose photospheric continuum was detected by the *EUVE* spectrometers. This paper is primarily concerned with the portion of the spectrum that lies between the neutral helium ionization edge at 504 Å and an effective cutoff by interstellar absorption near 700 Å. As in our EUV analysis of the B2 II star ϵ CMa, we found that line-blanketed model atmospheres are not capable of predicting an energy distribution which matches observations in all wavelength regions. Consequently, we derived two set of basic parameters for the star ($T_{\rm eff}$ = 24,800 K, log g = 3.7; and $T_{\rm eff}$ = 23,250 K, log g = 3.5), depending whether we accept the measured angular diameter, or require an exact agreement between models and the observed visual flux. For the higher $T_{\rm eff}$ model, the predicted EUV flux is in agreement with observations, while for the lower $T_{\rm eff}$ the star's EUV continuum is about 5 times brighter than the predictions. In either case, the star does not show the order of magnitude EUV excess that was seen in ϵ CMa. Neither model fits the data near 2200 Å, and additional photospheric opacity is proposed. The *EUVE* data also provide information concerning the low-density interstellar medium in the direction of β CMa. We derive a neutral hydrogen column density of $\sim 2 \times 10^{18}$ cm^{-2} and estimate a lower limit for the neutral helium column density of 1.4×10^{18} cm^{-2}. This indicates that along this sight line much of the hydrogen is ionized while the helium is neutral. The *EUVE* spectrum shows many strong photospheric absorption features, similar to that of ϵ CMa. Evidence for a stellar wind is seen in the O V 630 Å absorption feature.

There is special interest in β CMa because it is among the brightest of the β Cephei class of variables. The pulsations in this class of star manifest themselves primarily as periodic effective temperature changes. We find that the semiamplitude of the change is 108^{+31}_{-32} K for the primary period. This result is consistent with that derived from an analysis of the UV continuum by Beeckmans & Burger (1977), but our 68% confidence limits are significantly smaller than their 1 σ error bars. The general agreement implies that the pulsations do propagate between the layers where the optical and UV continua are formed and the layers where the EUV continuum forms, which is about six density scale heights higher in static models. The possibility that some pulsational energy deposition could occur within the outer photosphere is discussed. Our observations, taken over two time intervals separated by 70 days, resulted in the detection of the beat phenomenon owing to the three oscillation periods of β CMa.

Subject headings: ISM: abundances — line: identification — stars: early-type — stars: individual (β Canis Majoris) — stars: oscillations — ultraviolet: stars

1. INTRODUCTION

This paper reports on two observations of the variable star Mirzam, or β CMa (B1 II–III), using the three spectrometer channels of the *Extreme Ultraviolet Explorer* (*EUVE*). Even though the star is at a distance of 206 pc, it was detected with the long-wavelength (LW) spectrometer in the wavelength region $\lambda > 504$ Å. This EUV detection is primarily due to the position of β CMa in a galactic direction with very low interstellar column density. It is now the second early-type giant star for which the photospheric Lyman continuum radiation has been detected. The first was ϵ CMa (B2 II), which was discussed by Cassinelli et al. (1995) (Paper I). The two B giants ϵ CMa and β CMa rank first and second as the brightest stellar objects detected by the LW spectrometer on *EUVE*.

A comparison of these two well-studied stars is important because ϵ CMa was found in Paper I to have an unexpectedly large EUV continuum which exceeded the predictions of model atmospheres by more than an order of magnitude, both above and below the He I ionization edge at 504 Å. The doubling of the B star sample provides useful information about the ubiquity of the large EUV excesses in early-type stars, and it will allow for studies of the physical properties that can lead to EUV excesses. These two EUV data sets of B stars provide the best observational tests of

[1] University of Wisconsin-Madison, Department of Astronomy, 475 N. Charter Street, Madison, WI 53706; cassinelli@madraf.astro.wisc.edu, cohen@madraf.astro.wisc.edu.
[2] University of Wisconsin-Madison, Fusion Technology Institute, 1500 Johnson Drive, Madison, WI 53706.
[3] University of Oxford, Department of Astrophysics, Keble Road, Oxford OX1 3RH, England, UK.
[4] Present address: Department of Physics, Blackett Laboratory, Imperial College of Science, Technology and Medicine, London SW7 2BZ, England, UK.
[5] NASA/Goddard Space Flight Center, Greenbelt, MD 20771.
[6] Eureka Scientific, 2452 Delmer Street, Oakland, CA 94602.
[7] Space Sciences Laboratory, University of California-Berkeley, Berkeley, CA 94720.
[8] Max-Planck-Institut für Astronomie, Königstuhl 17, D-69117 Heidelberg, Germany.

model stellar atmosphere theory for early-type stars, because emergent flux in the spectral region below the Lyman edge is especially sensitive to model parameters.

These two objects have been well-studied in many wavelength regimes and both have angular diameter measurements from the Narrabri intensity interferometer (Hanbury Brown, Davis, & Allen 1974). Thus many observational properties can be accurately established. Table 1 presents the properties of the two stars, including ones derived in this paper. The two stars have nearly the same luminosity although β CMa has a smaller radius and a higher surface gravity. The effective temperature determination is somewhat uncertain (see § 3) but β CMa is about 3000 K hotter than ϵ CMa. In Paper I it was pointed out that IR continuum excesses provide a useful diagnostic of heating in the outermost regions of the stellar photosphere. For ϵ CMa the flux at 12 and 25 μm (as measured by *IRAS*) shows an excess of 10%–20% with respect to models (Paper I), whereas for β CMa the IR flux is closer to the theoretical predictions, and has only a small IR excess (see § 3 and Fig. 2).

Both ϵ CMa and β CMa are X-ray sources (Drew, Denby, & Hoare 1993) and have similar spectra and $L_X/L_{\rm Bol}$ values. The wind properties of the two stars are very similar, with both theoretically (Abbott 1982; Kudritzki et al. 1989) and observationally (Drew et al. 1993) determined mass-loss rates agreeing for the two objects. The similarities in wind and X-ray properties are important because the anomalously large Lyman continuum of ϵ CMa has been attributed to either NLTE effects associated with its wind (Najarro et al. 1995), or to the effects of X-rays impinging on the outer atmosphere (Hubeny & Lanz 1995a), Since the stars have excesses of different degree, the two stars will allow for interesting tests of the cause of the atmospheric heating. Knowledge of the X-ray emission is also important because of the effect that the X-rays have on the ionization conditions in the wind and upon the line emission from the cool portions of the wind (see Paper I).

The two early-type stars lie within 15° on the sky, and both are in a direction of very low interstellar density, often referred to as the β CMa tunnel. It would be interesting to know about differences in both the hydrogen and helium column densities along the two lines of sight. In this regard it is relevant that ϵ CMa has a measurable flux in the helium continuum shortward of 504 Å, while β CMa does not. The *EUVE* observations make it possible to better define both the spatial and physical properties of this unique interstellar region.

The two stars form a particularly useful pair for studying the pulsation properties of early-type stars. This is because β CMa lies in the β Cephei strip and pulsates, while ϵ CMa lies just beyond the red side of the strip and is not reported to show pulsations. A comparison between the EUV properties of the two stars will perhaps lead to new insight regarding the β Cephei pulsation mechanism, and may also help explain the excess EUV flux in ϵ CMa. Partly because β CMa is the brightest known member of the β Cephei class of variables it was the first to be well studied and it showed evidence for more than one period (Meyer 1934). Sterken & Jerzykiewicz (1993) present a historical review and an extensive summary of the properties of the β Cephei stars. The mechanism by which these stars pulse until recently had been one of the major puzzles of stellar interior theory. New opacities calculated by Iglesias & Rogers (1991) have shown the presence of an opacity peak due to iron ions that occurs at a temperature of about $10^{5.3}$ K. By accounting for the new opacities Moskalik & Dziembowski (1992) and Kiriakidis, El Eid, & Glatzel (1992) have shown that the pulsation of the β Cephei stars can be explained by the kappa mechanism.

The light curves of β Cephei stars lag behind the radial velocity curves by one-quarter period. This means that the stars have maximal brightness when the radius is smallest. Thus the variability is most directly explained as a periodic change in the effective temperature of the star. Consistent with this explanation of the variability is the fact that the

TABLE 1

STELLAR PARAMETERS FOR ϵ CANIS MAJORIS AND β CANIS MAJORIS

Parameter	ϵ CMa HD 52089	β CMa HD 44743
Spectral type[a]	B2 II	B1 II–III
m_V[a]	1.50	1.98
Distance[b] (pc)	188	206
θ_d[c] (mas)	0.80 ± 0.05	0.52 ± 0.03 (0.52, 0.59)[d]
$N_{\rm H}$[e] ($\rm cm^{-2}$)	0.7 to 1.2×10^{18}	2.0 to 2.2×10^{18}
$T_{\rm eff}$[f] (K)	$20{,}990 \pm 750$	$25{,}180 \pm 1130$ (24,800, 23,250)[d]
log g[g] ($\rm cm\ s^{-1}$)	3.2 ± 0.15	3.4 ± 0.15 (3.7, 3.5)[d]
$V \sin i$[h] ($\rm km\ s^{-1}$).....	35	30
L_X[g] ($\rm ergs\ s^{-1}$).....	1.8×10^{31}	1.2×10^{31}
$\dot{M}$[i] ($M_\odot\ \rm yr^{-1}$)	5.7×10^{-8}	3.5×10^{-8}
v_∞[i] ($\rm km\ s^{-1}$)	910	1220

[a] Bright star Catalog: Hoffleit & Jaschek 1982.
[b] Bohlin et al. 1978.
[c] Hanbury Brown et al. 1974.
[d] Range of values based on our two alternative atmosphere models (see § 3); in the first case θ_d is held fixed and in the second case m_V is held fixed.
[e] This work and Paper I.
[f] Code et al. 1976.
[g] Drew et al. 1994.
[h] Uesugi & Fukuda 1982.
[i] Theoretical calculations based on modified CAK theory, with line parameters taken from Abbott 1982 and the using the fitting formula of Kudritzki et al. 1989.

flux changes across a period are small in the visual region of the spectrum, while the flux changes are much larger at ultraviolet wavelengths. To first order this dependence of amplitude on wavelength can be understood by considering the emergent flux to approximate blackbody radiation. For a star with an effective temperature of about 23,000 K the visible region lies toward the Rayleigh-Jeans side of the spectrum where the monochromatic flux, F_λ, is proportional to the effective temperature. At the shorter UV wavelengths there is a much stronger dependence of F_λ on the temperature, so the changes in the effective temperature that arise from the pulsation should lead to a much larger flux variation. Observations in the EUV region of a β Cephei star are therefore especially interesting because the EUV lies well into the Wien side of the spectrum where there is an exponential dependence of the emergent flux on temperature; at 550 Å this corresponds to $F_\lambda \propto T^{13}$.

Observations of the flux amplitudes in the ultraviolet for β CMa have been analyzed by Beeckmans & Burger (1977), who derive the change in the brightness temperature of 180 ± 130 K. EUV observations should lead to a significant reduction in the large error bars associated with their analysis. However, in the EUV the stellar atmosphere opacity is much larger than in the ultraviolet. We will therefore be sampling conditions at a higher layer in the atmosphere, so in principle it is possible to learn more about the atmosphere than just the temperature variation, such as information about the damping of pulsational energy as a function of height.

In § 2 the *EUVE* observations and the flux and wavelength calibrations are described. A comparison between the emergent flux and the predictions of model atmospheres is made in § 3. The interstellar H I column density is also derived in this section. In § 4 the lines predicted by model atmospheres and by wind ionization calculations are used to identify most of the absorption features that occur in the spectrum. In § 5 we derive upper limits for the continuum and line fluxes below the helium edge at 504 Å. In § 6 the attenuation of the EUV radiation is used to derive information about the interstellar medium (ISM) toward the star. The variability of β CMa is assessed and compared with the behavior in other wavelength regimes in § 7. In § 8 we compare β CMa with ϵ CMa in regards to the properties of their outer atmosphere and winds, and discuss possible origins of heating of the outer atmosphere. There we also briefly summarize the results of this paper.

2. OBSERVATIONS AND DATA ANALYSIS

Observations of β CMa were carried out as part of the NASA *EUVE* Guest Investigator program in both Cycles 1 and 2. The observations were made from 1993 December 19 to 1993 December 22 and from 1994 February 27 to 1994 March 3 by the three spectrometers (SW, MW, LW) on *EUVE* (Bowyer & Malina 1991). These cover the EUV wavelength range from 70 to 740 Å. The average spectral resolution for the *EUVE* spectrometers is $\lambda/\Delta\lambda \sim 250$.

The *EUVE* Guest Observer software package (version 1.5, reference data version 1.9) was used for reduction and analysis. This includes the most recent wavelength calibration and effective area tabulation as of 1995 January. The data were time-filtered to include only the nighttime periods of the orbit. Periods of high detector background due to the South Atlantic Anomaly were also removed, as was a section of data which was corrupted because of a bad pointing direction. Deadtime corrections, necessitated by telemetry saturation effects, were calculated and applied. Effective exposure times vary slightly among the spectrometers but are 52,576 and 104,575 s for the LW spectrometer Cycle 1 and Cycle 2 observations, respectively. The LW raw spectrum for each observation is shown in Figure 1, along with the photon flux density at the top of the Earth's atmosphere for the combined data sets.

The two observations presented here were among the first made with the dithering maneuver, a procedure designed to reduce fixed pattern noise in the spectra caused by high spatial frequency nonlinearities in the readout of the microchannel plate detectors on *EUVE* (Vallerga et al. 1991). Due to the complexity of the β CMa spectrum, it is difficult to assess the success of the technique with these data alone. However, observations of white dwarf continua with *EUVE* using the dithering maneuver consisting of 35 pointings of HZ 43 indicate that the technique reduces the fixed pattern noise to less than 3% of the continuum (Dupuis et al. 1995). We therefore consider as statistically significant spectral features with a flux change greater than 5% of the continuum level, unless photon statistics warrant a more conservative threshold.

3. THE PHOTOSPHERIC CONTINUUM FROM β CMa

3.1. *Effective Temperature, Angular Diameter, and Surface Gravity*

In this section we discuss the basic atmospheric parameters for β CMa. We adopt an approach similar to that used in Paper I for ϵ CMa in which observed UV and optical properties are used to define a $T_{\rm eff}$ and log g. However, in the case of β CMa this approach presents us with an ambiguity that results in two determinations of the effective temperature; $T_{\rm eff} = 23{,}250$ K, and 24,800 K. Although we present arguments which tend to favor the lower value of

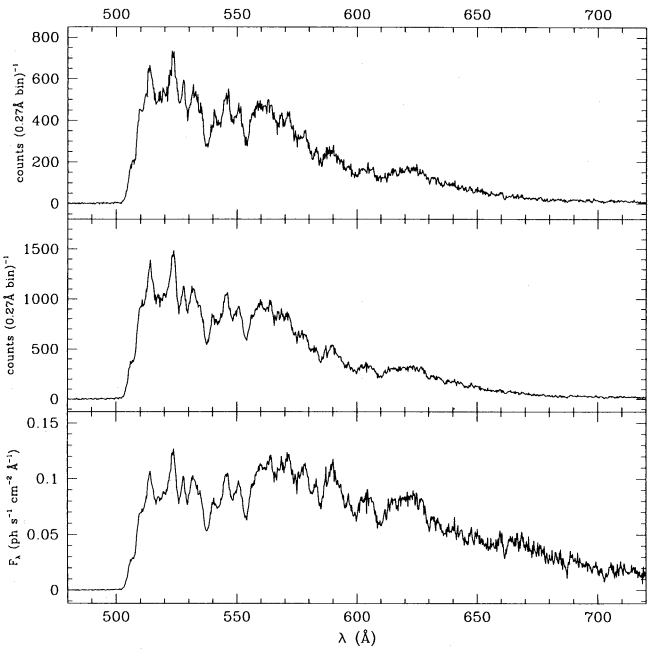

FIG. 1.—β CMa as observed in the *EUVE* LW spectrometer. We display total counts per 0.27 Å pixel in an effective exposure time of 55,695 s for (*a*) year 1 and 105,970 s for (*b*) year 2. In (*c*) we show the combined year 1 and year 2 data divided by the total effective exposure time, the detector effective area, and the bin size. This spectrum represents the photon flux density at the top of the Earth's atmosphere.

$T_{\rm eff}$, neither provides a consistent match with all of the observations and therefore we have to view the above values as the current limits for the derived effective temperature. In the rest of this section, we will explain why we are compelled to accept such a large uncertainty in the effective temperature. Nevertheless, we will also show that even this large range of $T_{\rm eff}$ does not significantly affect other astrophysical conclusions, in particular the derived interstellar hydrogen column density.

An effective temperature ($T_{\rm eff}$), angular diameter (θ_d), and surface gravity (log g) for β CMa are derived by comparing the observed mean energy distribution and published Balmer line profiles with predictions obtained from model stellar atmospheres computed with and without the assumption of local thermodynamic equilibrium (LTE). Line-blanketed model stellar atmospheres, assuming LTE and solar abundances, were computed using ATLAS9 (Kurucz 1992). Exploratory NLTE line-blanketed model stellar atmosphere calculations based on the TLUSTY code (Hubeny 1988; Hubeny & Lanz 1992, 1995b) were also carried out, but these models did not provide a better fit than the LTE models, so we will discuss only the LTE models in this section.

Optical fluxes are obtained from the 13-color photometry of Johnson & Mitchell (1975). Near-ultraviolet fluxes are taken from the *OAO 2* observation of Code & Meade (1979), and *S2/68* observations by Jamar et al. (1976). Using the calibration of Cohen et al. (1992), estimates of monochromatic fluxes at effective wavelengths of the J, H, K, L, and M filters are derived from ESO archive photometry collected by Bouchet, Manfroid, & Schmider (1991). Far-infrared fluxes are taken from the *IRAS* Point Source Catalog (1988). To define the far-ultraviolet wavelength range reaching down to the Lyman limit we use measurements from the *Voyager* satellite spanning a total of 49,271 s, with the observation commencing on 1991 April 29. The separate spectra were averaged into 10 phase bins (based upon the primary pulsation period of 0.2512985 days) and a mean spectrum was computed. Since β CMa's Lyman continuum emission shortward of 912 Å amounts to a negligible fraction (0.1%) of the star's total radiant output (as does the infrared contribution at $\lambda > 11084$ Å [0.5%]), $T_{\rm eff}$ is determined from the observed integrated flux between 912 Å and 11084 Å.

The first method of the effective temperature determination is based on the measured total flux and the measured angular diameter. The integrated flux, when normalized to the top of the stellar photosphere, using the interferometric angular diameter measured by Hanbury Brown et al. (1974), gives $T_{\rm eff} = 24{,}800$ K (Code et al. 1976). Various surface gravities (log g) were tried out for $T_{\rm eff} = 24{,}800$ K by comparing the corresponding Balmer lines (Hγ and Hδ, computed using Vidal, Cooper, & Smith 1973) broadening theory as coded in BALMER9) with observed profiles published by Watson (1972). The best agreement between observed and theoretical Hγ and Hδ profiles is obtained for log $g = 3.7$; it should be noted, however, that only the near-wings are fitted. As can be seen in Figure 2, the predicted energy distribution (for $T_{\rm eff} = 24{,}800$ K and log $g = 3.7$) is in good agreement with observed fluxes at $\lambda < 4000$ Å when normalized to the top of the Earth's atmosphere using the Hanbury Brown et al. angular diameter. However, departures between observed and normalized model fluxes at longer wavelengths are large; in particular, we consider the 10% discrepancy between the V-band fluxes to be unacceptable. The high surface gravity required at this effective temperature is also disturbing, considering that β CMa has a spectral type of intermediate luminosity class II–III.

The second method uses instead the measured flux in the V band. Adopting $V = 1.97$ as a mean for β CMa, estab-

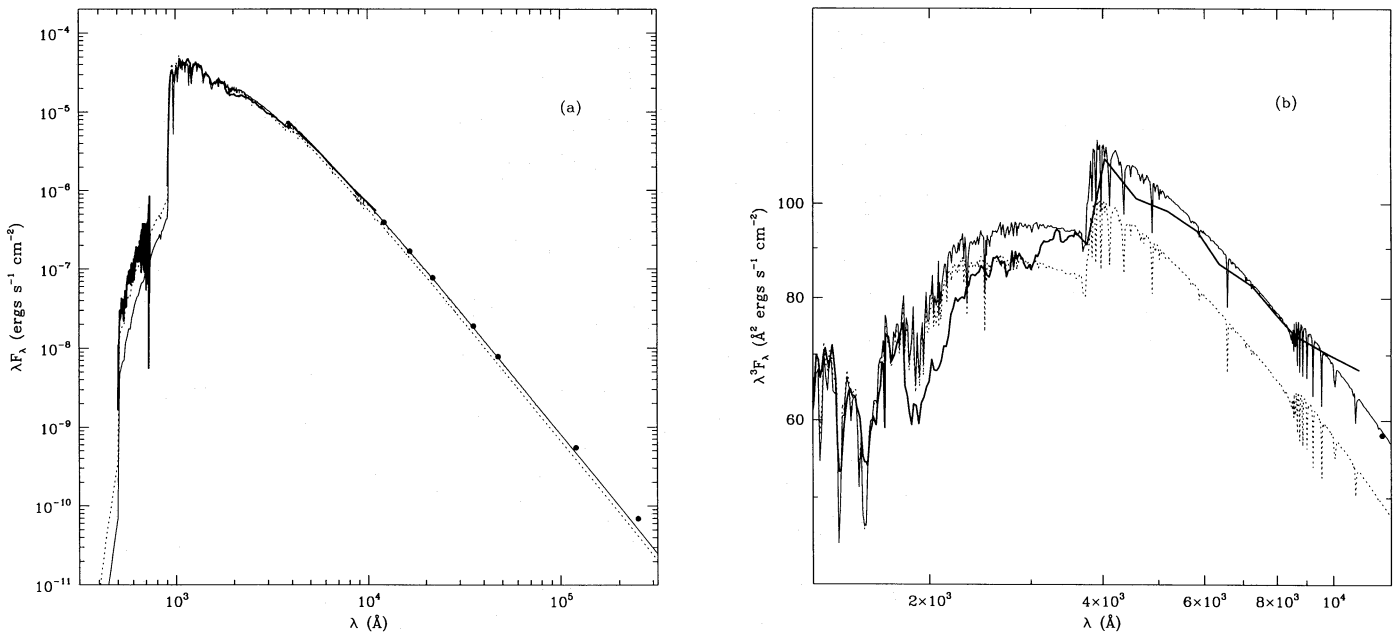

FIG. 2.—(*a*) The spectrum of β CMa in the form λF_λ vs. λ from EUV to IR wavelengths (*heavy solid line and dots*) with the two atmosphere models discussed in the text (solid line for the cooler model and dotted for the hotter model). Interstellar reddening is significant only in the EUV, where we have corrected the data assuming $N_{\rm H\,I} = 2 \times 10^{18}$ cm^{-2}. It is shown in § 3.2 that this correction is insensitive to the choice of atmosphere model. Note that there is an IR excess relative to either atmosphere model, and the data fall below both models in the region centered on ~2200 Å (*b*) Flux distribution of β CMa in the form $\lambda^3 F_\lambda$, giving an expanded view of the UV and optical spectrum and more clearly showing the difference between the two models. The designations of the models on the two panels are identical.

lished by Johnson et al. (1966), and also adopted by Perry, Olsen, & Crawford (1987), in their compilation of *ubvyβ* photometric standards, the calibration of Hayes (1985) gives a monochromatic V-band flux of 6.03×10^{-10} ergs cm^{-2} s^{-1} Å^{-1}. This differs by only 1% from the linear interpolation between adjacent fluxes deduced from Johnson & Mitchell (1975) 13-color photometry. A lower $T_{\rm eff}$ is deduced when the energy distribution is renormalized according to the angular diameter implied by reconciliation of the V-band flux with the model flux at the effective wavelength of 5454 Å; the lower $T_{\rm eff}$ prompts the calculation of a new model atmosphere which then results in a new angular diameter. Continuing the iteration until convergence is achieved results in $T_{\rm eff} = 23{,}250$ K. An almost identical result is obtained using J-band normalization and both a plausible and satisfactory fit to Hγ and Hδ is now achieved with log $g = 3.5$. The resulting model energy distribution, when normalized, is also compared with observations in Figure 2. It can be seen in Figure 2 that the normalized energy distribution for the $T_{\rm eff} = 23.250$ K model give a better representation of the observed energy distribution between 912 Å and 4 μm; it should be noted, however, that the model predicts too much flux at $\lambda \sim 2200$ Å. This is also a defect of the former model (see Fig. 2).

We favor the lower effective temperature because we find the V-flux discrepancy following from the first determination ($T_{\rm eff} = 24{,}800$ K) to be unacceptable. On the other hand, the lower effective temperature ($T_{\rm eff} = 23{,}250$ K) determination stipulates the angular diameter of 0.59 mas as compared with 0.52 ± 0.03 mas measured by Hanbury Brown et al. (1974). The discrepancy is thus slightly more than 2 σ. This 13% difference is not so very extraordinary in view of the history of comparisons made with the interferometric angular diameters since their publication over 20 yr ago. A relevant example to note is that Remie & Lamers (1982) compared their angular diameters derived for seven stars (using a method similar to but not identical with our own) with the Hanbury Brown data and found discrepancies ranging from 1% for ϵ CMa up to over 20% in the worst case (κ Ori). For β CMa Remie & Lamers derived an angular diameter larger than the direct measurement as we do here: they obtained 0.56 mas, as compared with our estimate of 0.59 mas. At first sight it may seem odd that Remie & Lamers's effective temperature for β CMa was given as 24,700 K, a value little different from Code et al.'s (1976) figure of 25,180 K based on the Hanbury Brown et al. angular diameter. The reason for this appears to be that Remie & Lamers assumed a nonzero reddening toward β CMa ($E[B-V] = 0.04$) while Code et al. treated it as negligible—as we now know it to be. If Remie & Lamers had used zero reddening they would have gotten the value that we did ($T_{\rm eff} \approx 23{,}250$ K). An analogous problem regarding their $T_{\rm eff}$ determination for ϵ CMa was discussed in Paper I.

There is an IR excess in the *IRAS* data (at 12 and 25 μm) relative to either atmosphere model. If the cooler model is indeed the correct one, then the IR excess is smaller and can be understood in terms of a temperature excess in the outer photosphere which would then also be the cause of the EUV excess (see Paper I). If the hotter model is correct then there is no such natural explanation for the larger IR excess because the observed EUV flux would be in agreement with the model prediction.

In summary: the present LTE line-blanketed model atmospheres are not capable of providing a consistent description of the emergent flux across all wavelength bands for early B giants. The case of β CMa illustrates this clearly. If we trust the measured angular diameter and measured total flux, we derive an effective temperature ($T_{\rm eff} = 24{,}800$ K), which yields a model flux consistent with observations in the UV and EUV region (except for the 2200 Å region), but it fails to provide an acceptable fit to the observed visual through infrared flux distribution. If we construct a model which fits the V-band flux, we are compelled to adopt a higher than measured angular diameter and a lower effective temperature ($T_{\rm eff} = 23{,}250$ K). The corresponding model atmosphere yields a good agreement with observations in the UV, optical, and near-IR region (except, again, the 2200 Å region), but fails to reproduce the observed Lyman continuum flux by a factor of about 5.

The NLTE model atmospheres are not yet able to remedy this situation. Nevertheless, the flux discrepancy at $\lambda \approx 2200$ Å indicates that there must be a significant missing opacity in the classical UV region. We stress this point because similar discrepancies between observations and theory were historically assigned to the well-known 2200 Å interstellar feature. In the present case we cannot invoke additional interstellar absorption. Therefore, the future models will have to address not only the Lyman continuum discrepancy, discussed at length in Paper I, but also the important 2200 Å discrepancy. Since the LTE models were constructed using the full line list of Kurucz (1992), it is unlikely that the discrepancy will be explained by merely adding new lines. Possible candidates are NLTE effects in the Fe II/Fe III ionization balance or a higher microturbulent velocity. We are currently working on generating new fully blanketed NLTE model atmospheres for ϵ CMa and β CMa to test the latter two hypotheses; the results will be presented in a future paper.

3.2. *The Lyman Continuum and the Estimation of the Interstellar Neutral Hydrogen Column*

In deriving an estimate of $N_{\rm H\,I}$ toward β CMa from the *EUVE* data the constraints available are the overall shape of the observed Lyman continuum emission and, to a lesser extent, its mean level. Although the data are not of a spectral resolution suited to interstellar line studies such as the one using *Copernicus* satellite data by Gry, York, & Vidal-Madjar (1985), which limited $N_{\rm H\,I}$ to between 1.0×10^{18} and 2.2×10^{18} cm^{-2}, the *EUVE* data cover the wavelength region in which neutral hydrogen has its largest cross section and therefore our data are very sensitive to small column densities. The observed energy distribution in the Lyman continuum is the consequence of interstellar attenuation acting on the emergent stellar flux, which cannot be determined independent of model assumptions. Nevertheless, we show here that the most reasonable models that can be considered now point to much the same result as Gry et al. (1985) obtained.

In Figure 3 we show the mean of both sets of *EUVE* observations of β CMa rebinned onto the same wavelength grid as that used for the ATLAS9 LTE models presented in the previous section. This facilitates comparison of the predictions of these models, after attenuation by a range of interstellar H I columns, directly with the data. In the first panel, the assumed stellar parameters ($T_{\rm eff} = 24{,}800$ K, log $g = 3.7$) are those consistent with the Hanbury Brown angular diameter. It can be seen that for these parameters,

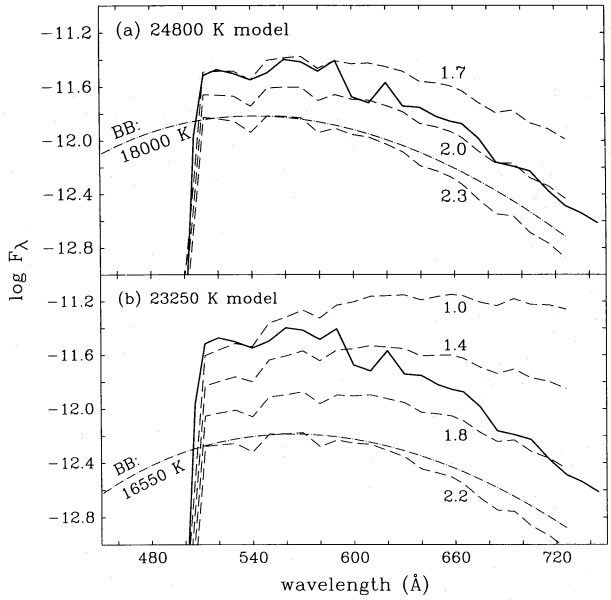

FIG. 3.—Comparisons between variously attenuated LTE line-blanketed model atmosphere predictions and the observed Lyman continuum emission from β CMa. The data (*dark solid line*) have been rebinned onto the same sparse grid as that used in ATLAS9. A dashed line style is used for the attenuated models. Each curve is labeled according to the attenuating neutral hydrogen column assumed (in units of 10^{18} cm^{-2}). (*a*) Comparison of different attenuations of the $T_{\rm eff}$ = 24,800 K, log g = 3.7 model with the data. (*b*) Comparison with the $T_{\rm eff}$ = 23,250 K, log g = 3.5 model. To illustrate the blackbody character of the model Lyman continuum, an appropriately attenuated blackbody curve is compared with one of the model curves in each panel.

the LTE model gives best agreement with observation with $N_{\rm H\,I} = 1.7$–2.0×10^{18} cm^{-2}. Indeed one might go further and construe that the comparison suggests the LTE model systematically underestimates the line-blanketing longward of about 580 Å by around 50% (0.2 logarithmically). Certainly there is more blanketing "structure" apparent in the data than in the model at these longer wavelengths.

However, it was argued above that the UV-optical energy distribution suggests the distinctly lower effective temperature of 23,250 K, together with an increased angular diameter and reduced surface gravity. In the second panel of Figure 3, we therefore compare the predicted, attenuated Lyman continuum flux for this new set of stellar parameters with the data. Clearly, there is no satisfactory match for any combination of predicted stellar continuum and interstellar absorption. To begin to achieve a *shape* of energy distribution resembling the observed energy distribution it is necessary to introduce the attenuation associated with $N_{\rm H\,I} \gtrsim 2.0 \times 10^{18}$ cm^{-2}.

It is encouraging to see that both model atmospheres yield reasonably consistent values of the interstellar column. Nevertheless, given the failure of model atmospheres to provide a consistent match of the observed flux for β CMa, we should not put too much faith on the predicted flux in the Lyman continuum. A crude, but less model-dependent, method is to use blackbody curves instead of model atmosphere predictions. This method was adopted in Paper I for determining the interstellar column toward ϵ CMa. Repeating the same procedure here (the reader is referred to Paper I for additional details), good agreement is achieved for a combination of blackbody temperature in the range (18,700 $\pm$ 400) K with an interstellar $N_{\rm H\,I}$ of (2.1 $\pm$ 0.1) $\times 10^{18}$ cm^{-2} (see Fig. 4). We note that this determination uses the same larger angular diameter as required by the 23,250 K LTE model. The error on the blackbody temperature is attributable in equal parts to the uncertainty in the absolute flux calibration of the *EUVE* data ($\pm$20%) and to uncertainty in placement of the blackbody envelope (the difference between curves [*a*] and [*b*] in Fig. 4, discussed in the figure caption). The derived blackbody temperature is also a little sensitive to the angular diameter scaling: the change on adopting the lower angular diameter measured by Hanbury Brown et al. is an increase of 300 K relative to that consistent with the larger diameter. However, it turns out that the error in the interstellar column arises primarily from the placement of the blackbody envelope with respect to the observed energy distribution.

In summary, the above comparisons all lead to an interstellar neutral hydrogen column density (2×10^{18} cm^{-2}) a little below the top of the range (1.0×10^{18} cm^{-2} to 2.2×10^{18} cm^{-2}) indicated by the interstellar absorption line study of Gry et al. (1985). Ultimately this agreement arises from the near or exact blackbody forms of the model stellar energy distributions adopted. A neutral column lying significantly beyond $\pm$10% of 2.0×10^{18} cm^{-2} becomes possible only after abandoning the plausible expectations that (i) the temperature change across the atmospheric layers producing the Lyman continuum is modest, (ii) the existing representation of line-blanketing in the Lyman continuum does not mislead very much more than is already suspected (panel [*a*] in Fig. 3), (iii) NLTE effects are not significant (this conclusion may be reached by consideration of the infrared continuum using reasoning similar to that applied in Paper I).

4. ABSORPTION LINES

A comparison of absorption features seen in β CMa and ϵ CMa is interesting for the light it sheds on differences in the temperature and ionization structure of the two stars and also for comparison of features that arise in the wind. We

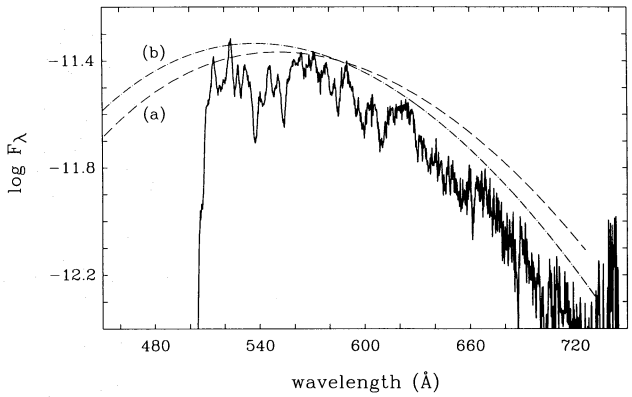

FIG. 4.—The observed Lyman continuum emission compared with (*a*) an equivalent blackbody of temperature of 18,500 K, attenuated by $N_{\rm H\,I}$ of 2.05×10^{18} cm^{-2}, (*b*) an equivalent blackbody temperature of 18,900 K, attenuated by 2.2×10^{18} cm^{-2}. The blackbodies are normalized to the higher angular diameter consistent with a stellar effective temperature of 23,250 K. The two curves (*a*) and (*b*) differ in underlying assumption: the placement of (*a*) is governed by the expectation that there is likely to be some decline in temperature outward through the atmosphere within the Lyman continuum forming layer (as is characteristic of existing model atmosphere calculations), while in (*b*) no point in the spectrum is allowed to go into net emission with the consequence that the implied run of temperature through the Lyman continuum forming layer is flat.

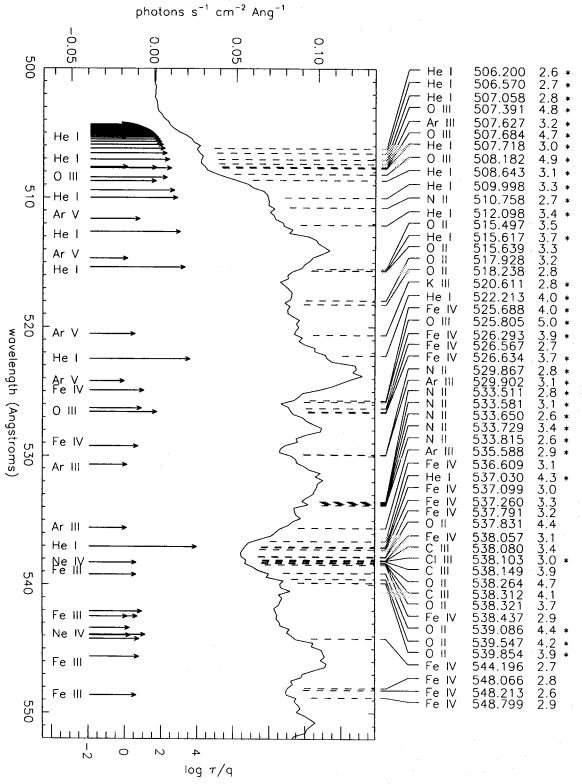

FIG. 5*a*

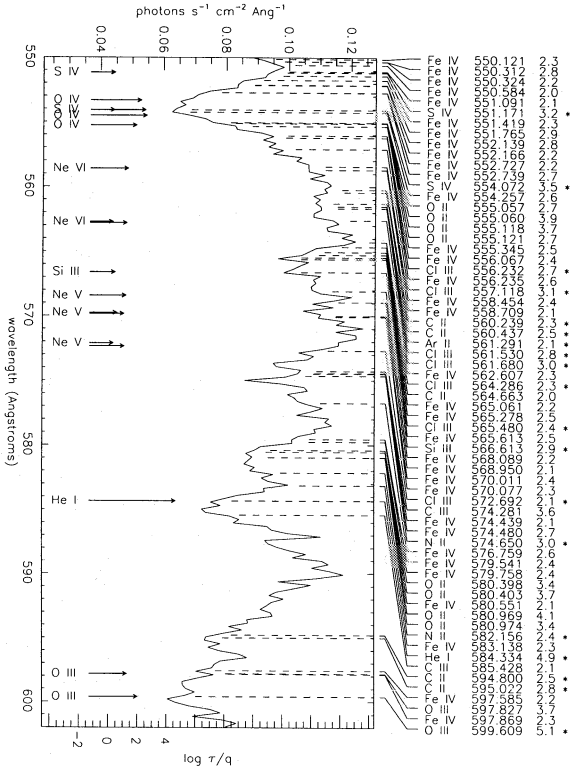

FIG. 5*b*

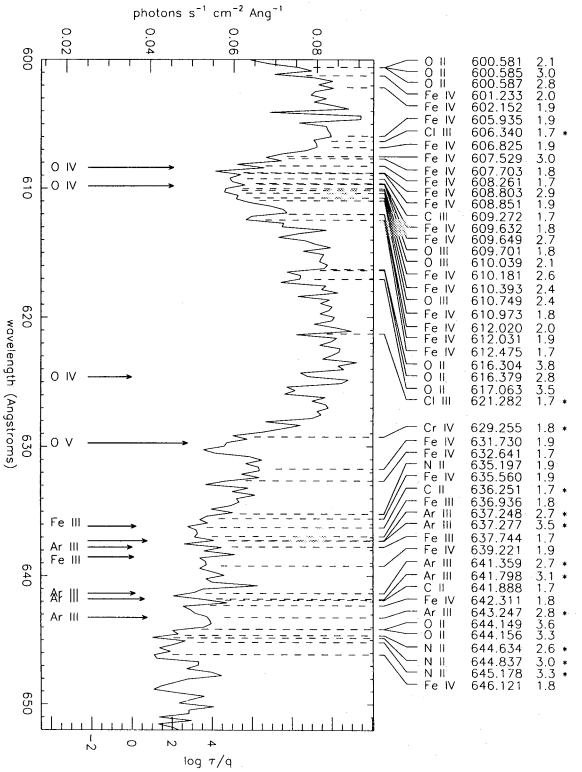

FIG. 5*c*

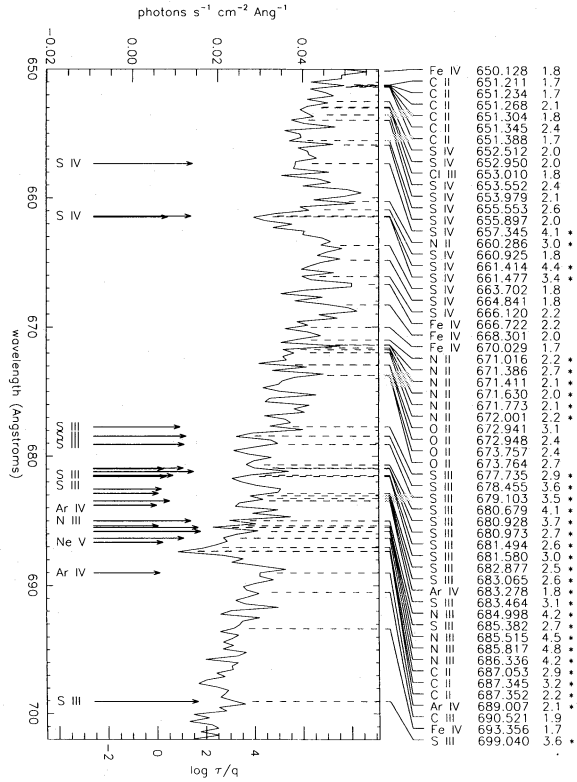

FIG. 5*d*

FIG. 5.—The LW spectrum of β CMa, the spectral lines which arise in the photosphere (*top*) and in the wind (*bottom*) are identified. See text for an explanation of the annotations.

calculated a synthetic spectrum from a 23,000 K, $\log g = 3.5$ LTE Kurucz model atmosphere and used it as a guide to the identification of photospheric absorption lines. We also made some comparisons to a TLUSTY 25,000 K NLTE synthetic spectrum. The model for the stellar wind contribution to absorption lines was calculated using the ionization balance and radiation transfer code described in MacFarlane, Cohen, & Wang (1994). Because of interstellar attenuation, the observed flux decreases rapidly with wavelength, so that the signal-to-noise ratio is only about 9 in a 1 Å bin at 700 Å. Therefore, not much can be said about the spectrum beyond that wavelength. However, the spectrum between 500 Å and 700 Å is rich with features.

Figures 5*a* to 5*d* show the LW spectrum of β CMa in ~ 50 Å segments, from 500 Å to 700 Å. The flux density above the Earth's atmosphere is plotted as observed by *EUVE*. The conversion from observed count rates to fluxes uses the instrumental sensitivity and wavelength calibration as discussed in § 2. The predictions of the photosphere model are shown along the top of the figure. Each line from the model is identified by the ion producing the line, the line wavelength, $\log r$ (the ratio of line center opacity to continuum opacity), and finally an asterisk is shown if the line is either a resonance line or one that originates from an excited level ≤ 3 eV from the ground. The lines expected to be formed in the wind are indicated along the bottom of the figure. The length of the arrow associated with each of the wind lines in Figure 5 is proportional to τ/q, where τ is the optical depth of the wind to line opacity, as given in Paper I, and the "ionization fraction," q, is the fraction of the element in the ionization stage producing the line. The scale of τ/q is shown on the right-hand side of the figure.

The most prominent absorption feature is the 504 Å edge, due to the ionization of neutral helium. The edge is displaced to the red by several angstroms, with the continuum level not reached until about 513 Å. This displacement is attributable to a confluence of neutral helium lines and to many resonance lines with transitions from the ground to high-lying bound states. There is also a strong O III resonance line triplet at 508 Å which contributes to the absorption. These oxygen ions exist in the stellar wind as well as in the photosphere. A similar longward displacement of the helium edge was also observed in ϵ CMa. Note also that a weak signal is detected shortward of 504 Å. This is due to the broad, shallow wings of the spectral response of the instrument and is discussed further in the next section.

In general, many of the same features we observe in β CMa are also seen in the spectrum of ϵ CMa, even though that star has an effective temperature that is several thousand degrees cooler, and also has a lower surface gravity. In this observation of β CMa, however, the continuum level and extent of the absorption features are better determined than for ϵ CMa because of our use of the dithering procedure, as described in § 2. Even so, β CMa shows a high degree of line blanketing.

Many of the absorption features are blends that often include several nonresonant lines of Fe IV. This is true of the broad absorption trough stretching from 514 to 523 Å that also contains lines of S IV, Ni IV, O II, and K III, as well as resonance lines of Cl III and Cl IV. The Lyman continuum is rich with absorption features of many abundant ions. We see absorption lines from all ion stages of oxygen from O II to O V. The O II arises in the photosphere, the O V arises in the stellar wind, and the O III and O IV have contributions from both the photosphere and the wind. The degree of line blanketing is quite high, but the amount of this blanketing which occurs in the wind is not clear.

The fit between the line data and the 23,000 K model is qualitatively quite good. We find that the strong features seen in the spectrum correspond to lines predicted to be strong in the atmosphere model. And there are no strong absorption features remaining unidentified, with the possible exception of the feature near 648 Å. We compared the fit to the absorption lines with the 23,000 K model to that with the 25,000 K model. The hotter model does not provide as good a match to the data as the cooler model. For example, several features in the data appear to be due to lines of O II, which are in the 23,000 K model but not the 25,000 K model.

Since the resolution of the instrument corresponds with a velocity which exceeds the wind terminal velocity it is not possible to identify wind lines by their line profiles. However, because the winds from hot stars are generally more highly ionized than their stellar photospheres we can attempt to identify wind features by their high degree of ionization. There are strong features near 554 Å and 609 Å which coincide with several O IV lines that are expected to be present in the stellar wind. In addition, some O IV may be expected to be present in the photosphere according to the 25,000 K atmosphere model, but very little according to the 23,000 K model.

The clearest case is that of the resonance line of O V at 629.7 Å, which is not expected to be present in the photosphere of a B1 star. In this region of the spectrum the apparent continuum may be depressed by heavy line blanketing. However, we can put a lower limit on the strength of the oxygen feature by conservatively choosing the continuum placement to be as low as is reasonable. Doing this we measure an equivalent width for the feature to be 336 ± 48 mÅ. We calculated a series of model equivalent widths for the absorption component of the O V 630 Å line using the SEI method of Lamers, Cerruti-Sola, & Perinotto (1987). The theoretical equivalent widths depend on the mass-loss rate, $\dot{M}$, the ionization fraction of O V, $q_{\rm O\,V}$, and on the wind terminal velocity, v_∞. For values of v_∞ between 400 and 1200 km s^{-1} we find an equivalent width of $\sim \frac{1}{3}$ Å is predicted for $\dot{M}\, q_{\rm O\,V} \approx 10^{-11}\ M_\odot\ {\rm yr}^{-1}$. If we have underestimated the continuum level, and thus the equivalent width of the 630 Å line, then the product $\dot{M}\, q_{\rm O\,V}$ could be as high as 10^{-10}, but only if $v_\infty \lesssim 400$ km s^{-1} and the line is saturated. A plausible value for $\dot{M}$ results if X-ray photoionization of oxygen in the stellar wind is important, as predicted by MacFarlane et al. (1994). Without X-rays $q_{\rm O\,V}$ is predicted to be negligible in the wind of β CMa, but with X-ray photoionization included in the calculations, we find $q_{\rm O\,V} \approx 10^{-3}$. The equivalent width measurement thus implies $\dot{M} \approx 10^{-8}$. This value is in good agreement with modified CAK wind theory result given in Table 1.

5. SPECTRUM BELOW 504 Å

We see a signal below the He I edge at 504 Å but much, if not all, of that signal can be attributed to photons scattered by the instrument from the longward side of the edge to the shortward side. Using the *EUVE* observation of ϵ CMa as a guide, one might have expected to see photospheric continuum radiation in the 400–500 Å range, and strong He II Lyman α emission at 304 Å. Several emission lines of highly ionized iron, which are associated with the X-ray producing

regions, as well as the O III 374 Å line, were also seen in the ϵ CMa observation, but are not seen in these observations. Here we discuss the probable causes of the nondetections of these features in β CMa and use them to deduce limits for the interstellar neutral helium column density, $N_{\rm He\,I}$, toward the star.

First we consider the He I ionization edge at 504 Å. Atmosphere models predict a decrement at the 504 Å edge of about two orders of magnitude. A larger jump than this could be due to absorption by He I in the ISM. So to determine a reliable value for the observed jump we have binned the data into 5 Å wide bins. For the observed flux on the longward side of the helium jump we use the average of the flux in the 510–515 Å band. The upper limit on the flux below the edge is calculated in the wavelength interval 495–500 Å and is equal to the signal from the scattered radiation. After having estimated the observed flux on both sides of the jump we find the observed decrement to be at least two orders of magnitude. This is about what the atmosphere models without ISM attenuation predict, so we conclude that the jump at 504 Å provides no reliable evidence for absorption by He I in the ISM.

In contrast with this result from the measured 504 Å decrement, the nondetection of the He II 304 Å line can be used to place strong limits on the neutral helium column density along the sight line to β CMa. This is because we can estimate the intrinsic luminosity of the 304 Å line from the similarities between β CMa and ϵ CMa. Both stars have similar UV spectra, and similar wind properties as based on theory (Table 1). Both have similar X-ray properties, with X-ray luminosities that differ by only about 25% (Drew et al. 1993). The X-ray luminosities are important because MacFarlane et al. (1995) show that for a sufficiently optically thick wind the 304 Å emission is governed almost entirely by the X-ray emission. This is because the line originates from the recombination of He III in the wind, and this ion is produced by photoionization by the EUV/X-ray radiation in the wind. Emission at 1640 Å would also originate from the recombination of He III, but this line would be unobservable against the much larger photospheric continuum in the UV.

Because of the similarity between observed wind and X-ray properties of the two stars, the luminosity of the 304 Å emission line emerging from the wind of β CMa should be comparable to the 2×10^{31} ergs s^{-1} that we derived in Paper I from the medium wavelength, MW spectrometer data of ϵ CMa. If the helium column density toward ϵ CMa is not negligible, then this value will be even larger, as will the corresponding upper limit for the sight line toward β CMa. We may thus ask how much interstellar opacity is required to fully attenuate the 304 Å line in β CMa if the line has the same intrinsic luminosity as that determined from observations of ϵ CMa?

From the MW spectrometer observations of β CMa we derive a 2 σ upper limit on the flux of the 304 Å line of 4.0×10^{-14} ergs s^{-1} cm^{-2}. This flux is 67 times less than expected for the assumed luminosity for the line. The decrease in the flux by this factor requires an ISM optical depth of 4.6 in the direction toward β CMa. The only important sources of interstellar opacity at 304 Å are neutral hydrogen and neutral helium. The hydrogen column density has already been well constrained in § 3 to the value 2.0×10^{18} cm^{-2}, which implies an optical depth of 0.6 due to hydrogen. This leaves $\tau = 4.0$ to be accounted for by helium, which has a photoionization cross section of 2.9×10^{-18} cm^{-2} at 304 Å. Therefore, we can place a limit on the interstellar neutral helium column density toward β CMa of $N_{\rm He\,I} \gtrsim 1.4 \times 10^{18}$ cm^{-2}. This is an interesting value because it is comparable to the column density of neutral hydrogen. Also this value is not very sensitive to the actual luminosity in the stellar emission line. If the line luminosity were assumed to be only $\frac{1}{3}$ of that seen in ϵ CMa, then the required column density of helium would be 1.0×10^{18} cm^{-2}.

No additional information can be found by considering the nondetections of the highly ionized iron lines and O III 374 Å that are seen in ϵ CMa. This is because their luminosities in ϵ CMa are much smaller than the He II 304 Å line, so even a very small ISM column density of He I would make them undetectable.

6. THE LOCAL INTERSTELLAR MEDIUM TOWARD β CMa

The He I column density derived in the previous section can be used to understand the structure of the β CMa tunnel feature in the local ISM. This rarefied interstellar tunnel, in which both β CMa and ϵ CMa lie, is 50 pc in diameter, and 300 pc long, and its general features have been described by Welsh (1991) and Gry et al. (1985). This elongated interstellar feature appears to be an extension of the region of low neutral hydrogen column density (often referred to as the "Local Bubble") which asymmetrically surrounds the Sun to 50 pc. This tunnel extension has been shown to possess a very low neutral gas density $n < 0.002$ cm^{-3} (Welsh 1991), thus making it one of the lowest interstellar density regions yet measured in our Galaxy.

In § 3 we have derived $N_{\rm H\,I} = 2.0 \times 10^{18}$ cm^{-2} toward β CMa ($d = 206$ pc), which is to be compared with that of $N_{\rm H\,I} = 9 \times 10^{17}$ cm^{-2} toward the star ϵ CMa ($d = 188$ pc) (Paper I). These two stars are only 15° apart on the sky and have very similar distances, yet have interstellar neutral hydrogen column densities that differ by a factor of 2. There are two possible explanations for this column density difference: (*a*) an inhomogeneity in the neutral gas near the Sun (the Local Cloud) between us and these two stars, or (*b*) an additional interstellar cloud with an angular extent less than 15° in the line of sight toward β CMa. We think explanation (*a*) is unlikely based upon the interstellar hydrogen column density measurements toward stars with $d < 100$ pc in this general galactic direction (i.e., α CMi, α CMa, MCT 0501−2858 and MCT 0455−2812), all of which have $N_{\rm H\,I} < 1.1 \times 10^{18}$ cm^{-2} (Linsky et al. 1993; Frisch 1994; Vennes et al. 1993). Hence, it would appear that the local interstellar cloud ($d < 10$ pc) is of remarkably uniform column density in this galactic direction. Also, our lower limit of neutral helium of $N_{\rm He\,I} = 1.4 \times 10^{18}$ cm^{-2} is inconsistent with accepted Local Cloud values of $N_{\rm He\,I} = 1 \times 10^{17}$ cm^{-2}. Interstellar helium absorption at these levels are also inconsistent with measurements toward other nearby ($d < 30$ pc) stars. Therefore, we postulate that there is additional interstellar gas of neutral column densities, $N_{\rm H\,I} = 1 \times 10^{18}$ cm^{-2}, $N_{\rm He\,I} \gtrsim 1 \times 10^{18}$ cm^{-2} and angular extent less than 15° in the direction of β CMa.

The actual physical state of this cloud was initially postulated by Gry et al. (1985) to be highly ionized. Using a standard Strömgren H II region model, together with the observed S II/S III line ratio, Gry et al. obtained a total ionized hydrogen column density of $N_{\rm H\,II} = 1.8 \times 10^{19}$ cm^{-2}, located in a cloud of some 40–90 pc in length toward

TABLE 2

KNOWN OPTICAL AND UV PERIODS

Period	Optical (Shobbrook 1973)	UV (Beeckmans & Burger 1977)
P_1 (days).....	0.2512985 ± 0.0000003	0.2512985
P_2 (days).....	0.25003 ± 0.00004	0.2500225
P_3 (days).....	0.23904 ± 0.00004	...

β CMa. If we assume a normal cosmic abundance ratio of 0.1 for the total helium to total hydrogen column density, then the Gry et al. value for $N_{\rm H\,II}$ implies a helium column density of $N_{\rm He\,I} = 2 \times 10^{18}$ cm^{-2}. This value is consistent with the lower limit of $N_{\rm He\,I} > 1.4 \times 10^{18}$ cm^{-2} that we derived in § 5. Our inference that there is a column density of neutral helium comparable to that of neutral hydrogen toward β CMa therefore supports the view that the low neutral hydrogen column density results from the ionization of hydrogen rather than from an absence of gas. Also the comparison between the column densities that we are finding and those discussed for the Local Cloud in the previous paragraph indicates that the very low density in the Local Cloud does not extend as far as β CMa. Similar conclusions cannot reached in the case of ϵ CMa because for that star we found no evidence for interstellar neutral helium, and thus there is toward ϵ CMa either a low total density or a high degree of ionization for both helium and hydrogen.

If the gas detected toward β CMa is photoionized, it is more likely close to the early B stars β CMa and ϵ CMa, where the radiation field is strongly dominated by the hydrogen ionizing photons longward of 504 Å, rather than in the Local Bubble where the radiation field due to the 10^6 K gas and a number of hot white dwarfs lead to substantial helium ionization (Cheng & Bruhweiler 1990). Hence we concur with the findings of Gry et al. (1985) that there is a substantially ionized gas cloud, most probably in the form of an H II region, actually surrounding β CMa. Why such an ionized cloud should be associated with and near β CMa and not ϵ CMa is still not clear. However, high-resolution absorption observations of the lines of sight toward both ϵ CMa and β CMa, using the Goddard High Resolution Spectrograph on *HST*, should help clarify the present interpretation of this unusual interstellar line of sight (Gry 1995).

7. VARIABILITY

Optical variability has been observed in β CMa for the past 90 yr and UV variability was measured by several satellites in the early 1970s. Three periods, all close to 6 hr, are seen in the data of Shobbrook (1973) (see Table 2). The magnitude of the variability is small (0.02 mag in the visible) but is seen to increase toward shorter wavelengths. This wavelength dependence is expected if the variability is due primarily to changes in temperature. Beeckmans & Burger (1977) find that the wavelength dependence of the variability is especially noticeable for the primary pulsation period. Because we are observing this β Cephei pulsator in the EUV, which is on the Wien side of the stellar spectrum, the variability should be more pronounced, unless the pulsations are damped out before reaching the upper layers of the atmosphere where there is maximal contribution to the Lyman continuum formation.

To investigate the time variability in the *EUVE* data we created a light curve from the spectrum between 500 Å and 700 Å, filtering the data to remove times of bad pointing and sampling and subtracting the background count rate as we did for the spectral reduction (see § 2). We calculated formal errors based on photon counting statistics for the source and background, but did not account for systematic errors. There could be a systematic contribution to the total uncertainty due to spacecraft/detector instability, imperfect deadtime corrections, and the effects of dithering. The resulting light curve consists of a 3 day long segment separated by 70 days from the second observation spanning 6 days. The count rate was averaged over bins of 500 s duration. The light curve was tested against the hypothesis of a constant source by calculating the χ^2 statistic for the data and a source model with a constant flux. This hypothesis could be rejected with a very high confidence level ($\chi^2_\nu \approx 5$ for $\nu = 475$). We next searched for periodicities in the data by calculating a power spectrum (see Fig. 6). The power spectrum revealed a strong signal near 6 hr, as well as some higher frequenccy power. Ultimately all of the high-frequency power could be attributed to the intrinsic variability (based upon the three-period model described below) and aliasing due to the uneven sampling of the data. In Figure 6*b* we show the power spectrum of the residuals from the best-fit model. All of the statistically significant high-frequency power has gone away, except for one peak near

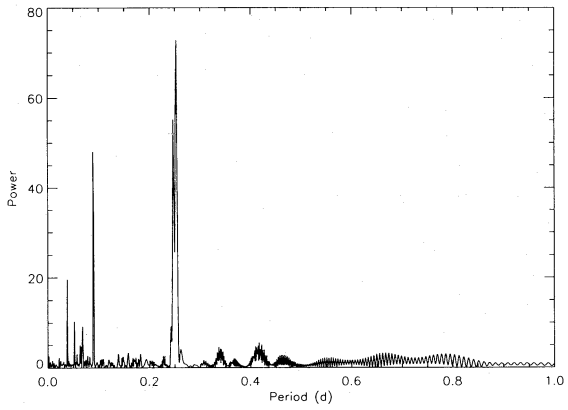

FIG. 6*a*

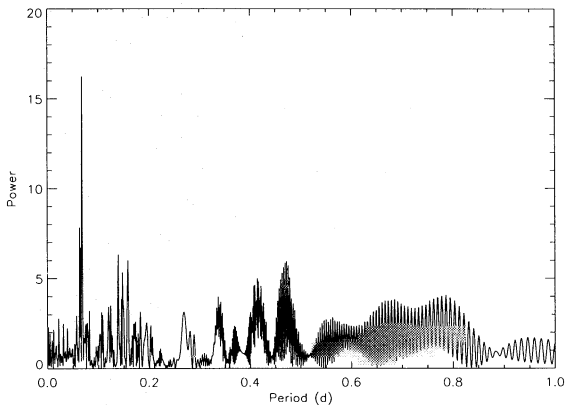

FIG. 6*b*

FIG. 6.—(*a*) The power spectrum of the 500–700 Å light curve for years 1 and 2. The peak near 0.25 days is due to the intrinsic variability of the star, but the individual components of the variability have such similar periods that the structure in this peak cannot be resolved. (*b*) The power spectrum of the residuals from the best three-period fit to the light curve. Note the much smaller scale on the *y*-axis. The only significant peak in this power spectrum (near 90 minutes) can be attributed to the orbital period of the satellite.

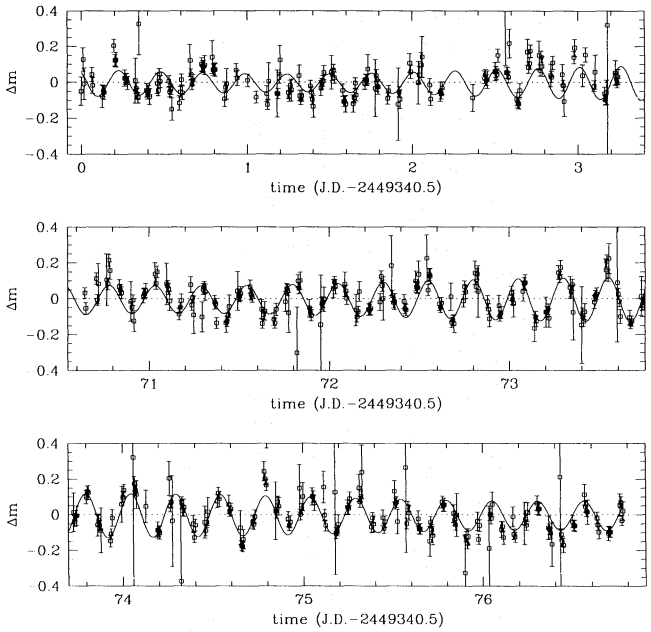

FIG. 7*a*

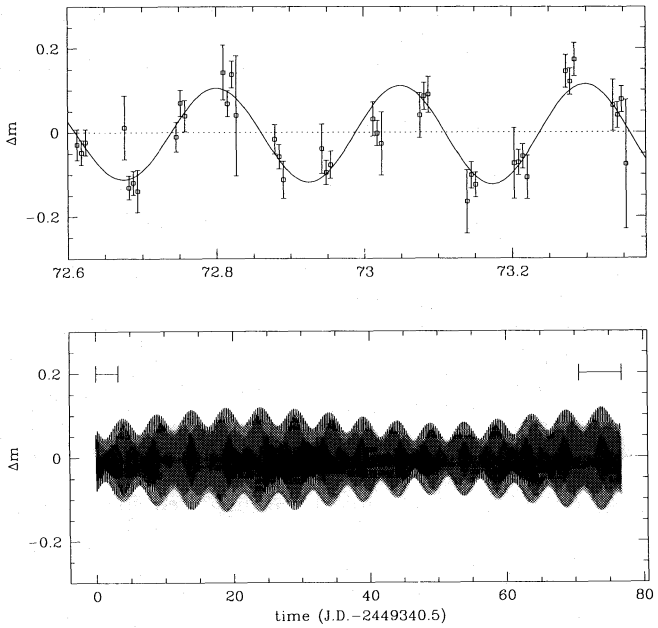

FIG. 7*b*

FIG. 7.—(*a*) The light curve constructed from the wavelength interval 500–700 Å with 500 s bins. The best-fit, three-period model is shown as the solid line. Note that the amplitude of the model changes as a function of time. This is evidence of the beat phenomenon. (*b*) The top panel displays one small section of the fitted light curve and the bottom panel shows the full three-period model. The horizontal bars indicate the epochs for which we have data. The beat periods among the three separate stellar pulsation periods can be readily seen in this figure. Better coverage of the long beat period will be required to more accurately constrain the model parameters.

90 minutes which is attributable to the spacecraft orbital frequency.

The best single sine wave model, at the frequency indicated by the power spectrum, resulted in a significantly better, although not adequate, fit to the light curve compared to the constant source model. We know that several periods are visible in the optical and UV, but the *EUVE* data do not, however, span a long enough baseline to resolve the individual components in the peak of the power spectrum. In order to determine the periods and the amplitudes of the separate components we had to fit models to the light curve.

We used the sinusoidal function described by Beeckmans & Burger (1977) to model the *EUVE* light curve. This model describes the change in magnitude as a superposition of the sum of a sine and cosine function for each separate period as

$$-\Delta\mathrm{mag} = \sum a_i \sin\frac{2\pi t}{P_i} + b_i \cos\frac{2\pi t}{P_i} + c\ ,$$

where

$$a_i = A_i \sin\frac{2\pi t_{0,i}}{P_i}$$

and

$$b_i = A_i \cos\frac{2\pi t_{0,i}}{P_i}\ .$$

Here $t_{0,i}$ is the epoch of maximum light, P_i is the period, and A_i is the amplitude of the variability. First we fit a two-component sinusoid ($i = 1, 2$) as those authors did, and this improved the fit relative to the single sine wave. Adding a third period further improved the fit. Figure 7 shows the light curve and the best-fit model. The periods we derive are consistent with those found in the optical, although the best fit P_1 is less than that seen in the optical and UV. The value of P_1 derived from optical and UV data is consistent with the value we derived from the *EUVE* data at the 99% confidence level. The amplitude of the dominant period is larger than that in the UV but the amplitudes of the other two periods are comparable (see Table 3). We calculated the range of solution space according to the $\Delta\chi^2$ criterion for joint probability distributions (Lampton, Margon, & Bowyer 1976). Holding P_3 constant (since the overall solution is insensitive to the details of the third period), we have four parameters of interest (two periods and two amplitudes) and the quoted error bounds in Table 3 are the

TABLE 3

BEST FIT LIGHT CURVE MODEL PARAMETERS

	BEST MODEL				RANGE (LOW:HIGH)			
	PERIOD (d)	t_0[a] (d)	Δmag	ΔT_b (K)	Period (d)	t_0[a] (d)	Δmag	ΔT_b (K)
P_1.....	0.251065	0.1043	0.084	108	0.2509955:0.2511318	0.0839:0.1174	0.059:0.108	76:139
P_2.....	0.249952	0.2017	0.020	26	0.249609:0.250082	0.1534:0.2519	0.011:0.046	14:59
P_3.....	0.239035	0.0517	0.022	28	0.239035[b]	0.0517[b]	0.022[b]	28[b]

[a] The epoch of maximum light (JD-2,449,340.5)

[b] Fixed.

68% confidence limits defined by $\Delta\chi^2 = 4.72$. The χ^2 value for the best-fit three-period model is not ideal ($\chi^2_\nu \approx 2$), indicating that either there is some intrinsic aperiodic variability or, more likely, we have underestimated the uncertainties due to our neglect of instrumental systematic errors.

ROSAT WFC observations have also been reported as showing evidence of time variability in β CMa's Lyman continuum emission (Hoare, Drew, & Denby 1993). However, in that case the detection was of marginal statistical significance (Δmag = 0.04, with comparable error bars) and, indeed, most likely on the "wrong" period (P = 2.98 hr), if real. It is difficult to explain this in view of the larger amplitude of variation suggested by the *EUVE* data, which should have been apparent to the WFC if present. Perhaps interference between the different periods and data sampling limitations resulted in a quasi-steady signal in the WFC that could have suggested an erroneous period.

We can calculate the brightness temperature variation for each component of the pulsation from our derived values of the amplitudes. We find for the primary period a change of 108^{+31}_{-32} K (quoted uncertainties represent the maximum extent of the 68% confidence limits) and a smaller change for the other periods. Beeckmans & Burger (1977) derived changes in the effective temperature from the variation in the 1810 Å flux. In the UV the effective temperature and the brightness temperature are very similar, so their results are directly comparable to ours. We find a smaller temperature variation than those authors, but our results fall within their error determinations. We conclude therefore that while there may be some damping of the pulsations between the layers of optical/UV continuum formation and those of Lyman continuum formation, the pulsations do propagate to very high layers of the atmosphere. In fact, the Lyman continuum is formed $\sim$6 scale heights above the layer of formation of the optical continuum in static models, so we are observing the propagation of the pulsations over a large spatial scale. Furthermore, like Beeckmans & Burger (1977), we see a trend of increasing changes in the flux with decreasing wavelength for the primary pulsation period only. We can examine the variability due to the primary period by subtracting the best-fit model predictions for the second and third periods from the data. The folded light curve for P_1 is shown in Figure 8, along with the best-fit model for P_1. Although there is a great deal of scatter, the sinusoidal model seems to provide an adequate fit to the shape of the light curve.

To examine the behavior of the brightness change as a function of wavelength within the *EUVE* bandpass, we constructed two separate light curves from narrower wavelength intervals: 500–550 Å and 550–700 Å. We fit these

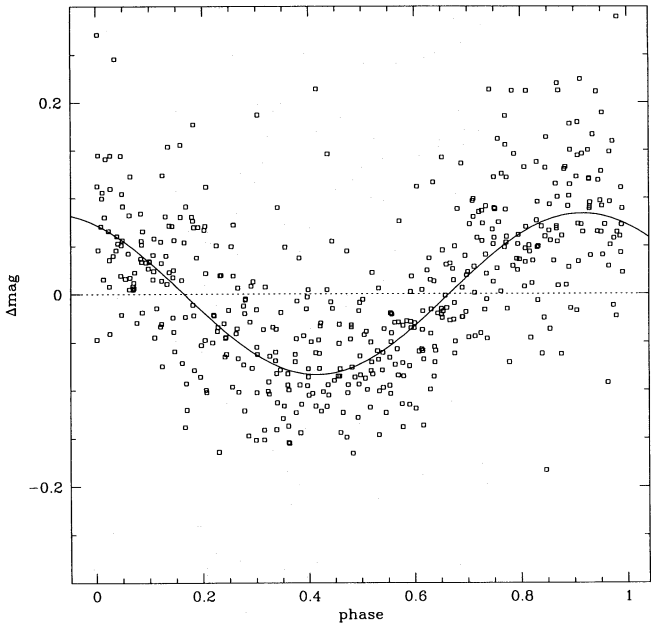

FIG. 8.—The folded light curve constructed from the wavelength interval 500–700 Å with the contributions from P_2 and P_3 subtracted from the data. The best-fit model is shown as the solid line.

light curves with the same sinusoidal model described above, but with the periods fixed at the best-fit values derived from the full light curve. If the pulsation can be primarily understood in terms of just a temperature change, then we should see a larger variability amplitude in the shorter wavelength light curve.

Indeed, the flux variations for the dominant period are larger below 550 Å than above 550 Å (see Table 4). The increased flux variation is slightly greater even than that which would be expected from a constant change in temperature, with the temperature change derived from the $\lambda < 550$ Å light curve being marginally larger than that derived from the $\lambda > 550$ Å light curve. If further observations confirm this result, it would be consistent with the idea that the pulsations are somewhat damped out as they propagate through the extreme outer photosphere. This is because the opacity increases with wavelength in the Lyman continuum, so that at $\lambda > 550$ Å the $\tau = \frac{2}{3}$ point is higher in the atmosphere than the corresponding optical depth below 550 Å. The Lyman continuum radiation, therefore, is determined by the temperature at increasingly higher layers in the photosphere as we look at longer wavelengths.

Another way to investigate the wavelength dependence of the variability is by constructing a phase-weighted spectrum which shows the difference between the spectrum of

TABLE 4

BEST FIT[a] MODEL PARAMETERS FOR THE TWO SEPARATE LIGHT CURVES

	P_1		P_2		P_3	
WAVELENGTH	Δmag	ΔT_b (K)	Δmag	ΔT_b (K)	Δmag	ΔT_b (K)
$\lambda > 550$ Å.....	$0.075^{+0.007}_{-0.010}$	101^{+9}_{-13}	$0.023^{+0.009}_{-0.007}$	32^{+12}_{-10}	$0.019^{+0.005}_{-0.007}$	25^{+7}_{-9}
$\lambda < 550$ Å.....	$0.096^{+0.007}_{-0.008}$	118^{+8}_{-10}	$0.016^{+0.007}_{-0.008}$	19^{+9}_{-9}	$0.027^{+0.005}_{-0.006}$	33^{+6}_{-5}

[a] The uncertainties represent the extent of the 68% confidence limits for a model with three free parameters of interest (Lampton et al. 1976).

the star in the bright phase and the dim phase of the pulsation cycle. This will give us a higher resolution view of the wavelength dependence of the change in temperature. Based upon the best-fit model we can assign a phase (with respect to P_1) to each photon collected. Using this information we constructed a spectrum in which the sine of the phase of each photon is summed in each wavelength bin. This produces what is essentially a difference spectrum, but with photons arriving at intermediate phases also included in the summation, albeit with lesser weight than those which arrive at the extremes of the brightness variation. If there is very little variability, then the photons from $\phi = \pi/2$ will nearly cancel the photons from $\phi = 3\pi/2$. If, on the other hand, more photons arrive near $\phi = \pi/2$ than near $\phi = 3\pi/2$, then a positive phase-weighted spectrum will be found. We then compute the ratio of the phase-weighted spectrum to the full spectrum to investigate the relative variability of the spectrum at each wavelength (see Fig. 9). If the variability has no wavelength dependence, then this ratio will be constant.

It can be seen in the bottom panel of Figure 9 that the variability does indeed increase toward shorter wavelengths. We fit a model of the brightness temperature change to the data displayed in the bottom panel. We find a slightly lower temperature than that derived from the light curve for P_1 and we find no need to introduce a wavelength dependence to the model temperature difference, although there is a wavelength dependence for the brightness variation. These results are not as reliable as the light curve analysis because we have no way of accounting for the second and third periodicities. The phase-weighted spectrum does have advantages, however, for examining spectral variability at high resolution. It is possible, for example,

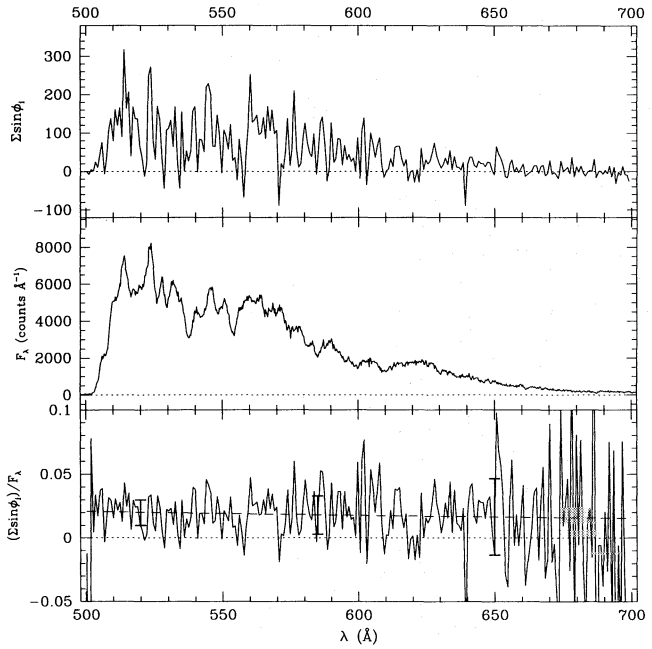

FIG. 9.—The phase-weighted spectrum is shown in the upper panel. In the middle panel we show the full spectrum (in raw counts per Å), and in the lower panel we shown the ratio of the phase-weighted spectrum to the full spectrum. The dashed line in the bottom panel represents the best blackbody fit to the data. The temperature change in the model is 48 K, but this value is lower than the true change because of the presence in these data of variability attributable to the second and third periods. Typical 1 σ uncertainties for 1 Å bins are indicated at three different wavelengths.

that some of the absorption features vary less than the continuum (see, e.g., the feature near 555 Å). This could also be interpreted in terms of damping of pulsations in the extreme outer photosphere, as the line centers are formed at higher photospheric layers than is the continuum. Improving the signal-to-noise ratio of the phase-weighted spectrum through the acquisition of more data would be useful for analyzing spectral line variability.

Pulsational damping in stellar atmospheres has been well studied in the case of the cool Mira variables by Bowen & Willson (1991). For those stars the damping of the pulsation plays a major role in the driving of their massive winds. In the case of the β Cephei stars, the topic of damping of pulsational energy has not received much attention. Most of the pulsation studies have dealt with mode analyses and the derivation of the periods of oscillation. The details of the properties of the atmosphere have not been an important aspect of such studies. However, we now have new data pertaining to the propagation of the β Cephei pulsations within the stellar atmosphere. We also have an unsolved problem involving flux excesses in the Lyman continuum. It is conceivable that as the pulsations are partially damped in the extreme outer layers of the photospheres of B stars, the mechanical energy is converted to heat which may have the effect of changing the temperature structure of the Lyman continuum formation layer. Only a modest amount of heating (a few percent) would be required to explain the observed flux excesses in the Lyman continua (and IR continua) of β CMa. This general scheme may also be able to account for the observed EUV excess in the ϵ CMa. That star is not observed to undergo β Cephei pulsations, but it is located very close to the β Cephei instability zone in the H-R diagram (slightly to the red side). This implies that the opacity-related instability exists in ϵ CMa as well but the instability zone is slightly deeper within the star's interior. Perhaps residual damping of the pulsations occur in the outer atmosphere of ϵ CMa and could lead to the observed large Lyman continuum excess in that star.

8. CONCLUSIONS

We have obtained 150 kiloseconds of spectroscopic data for β CMa with the *EUVE* satellite. There is only one other hot star known that has a significant flux in the long-wavelength spectral band of *EUVE*, ϵ CMa. The two stars have very similar properties, and this leads to especially fruitful comparisons. We have deduced that β CMa does not show the factor of 30 excess relative to models in its photospheric Lyman continuum that is seen in ϵ CMa. However, we cannot state with certainty whether β CMa shows a significant Lyman excess or not, because we derive two different effective temperatures. The higher effective temperature, along with no EUV excess, is obtained if we take the Narrabri angular diameter observation as certain. If instead we allow for a 2.3 σ error in the angular diameter data, and base our estimate of the effective temperature on model fits to the best data available from the UV and visual continuum—stressing especially the need to reproduce the measured V magnitude—we derive a lower value of $T_{\rm eff}$. Using the lower value would lead us to conclude that β CMa also has an excess EUV continuum flux, which leads to a natural explanation for the observed IR excess. This lower $T_{\rm eff}$ model also predicts a more reasonable surface gravity than the higher $T_{\rm eff}$ model and reproduces the O II lines, which are seen in the spectrum.

The tentative conclusion that there is an EUV excess is of great interest for considerations of the effects of B stars on the ionization of the ISM. EUV observations are available for only two B stars. Hence nearly all of our predictions of the ionizing radiation from B stars comes from inferences based on UV and optical data and models of the Lyman continuum flux. It is presently not possible to use direct observations to find other B stars that show such a large EUV flux. Thus we must now rely on indirect methods to determine if many other B stars show EUV excesses. B stars can have small H II regions around them, and the analysis of the Hα flux is a well-known way to study the EUV radiation from hot stars. Kutyrev & Reynolds (1995), have found that two out of eight B stars show a more luminous H II region than expected from predictions based on the effective temperatures of the stars. They also note that an excess of EUV radiation cannot be ruled out for the other stars in their sample because the nebulae could be mass bounded (i.e., have too little mass to absorb all of the EUV radiation from the central star). In Paper I we noted that the IR continuum near 12 μm forms at about the same height in the atmosphere as does the 500–700 Å emission. Observations of the IR continuum of B stars are therefore clearly another useful way to study temperature enhancements in the outer atmosphere of B stars. The *ISO* satellite should provide new information about the ubiquity of temperature, and hence EUV, excesses in the outer atmospheres of B stars.

The ISM is more opaque in the direction of β CMa than in the direction of ε CMa, with a neutral hydrogen column density about twice that estimated for ε CMa. We also have been able to place a 2 σ lower limit on the neutral helium column density on the β CMa sight line of 1.4×10^{18} cm^{-2}. This large value explains why no radiation is observed below 504 Å in β CMa. This limit for $N_{\rm He\,I}$ is much larger than the value for the ε CMa sight line, implying that there is a cloud component toward β CMa, which is not seen toward ε CMa, where hydrogen is highly ionized compared to helium.

We have found that the line spectrum of β CMa is very similar to that of ε CMa. The absorption line spectra of ε CMa and β CMa both show a high degree of line blanketing and line blending. Many of the same features are seen in the two stars, even though ε CMa has a significantly lower effective temperature. This may be additional evidence that the lesser of the two $T_{\rm eff}$ values that we derived for β CMa is the more correct one, and that therefore the star does have an EUV excess relative to currently available model atmospheres. Another similarity between the absorption spectra of the two stars is the presence of the O V 630 Å line. This ion stage is too high to be produced in the photosphere of either star and as such is the best evidence for a fast wind from the two stars. The measured equivalent width of this feature in the β CMa spectrum is consistent with the accepted mass-loss rate, terminal velocity, and ionization fraction of O V assuming that X-ray photoionization is an important effect in the stellar wind.

The most exciting aspects of our study of β CMa arise from its variability. It is the brightest of the β Cephei class of variable stars that has recently been a subject of much interest to stellar interior theorists. However, because the variability of these stars is small at visible wavelengths, there are large uncertainties in the amplitude of the variation. Since the variation is primarily due to a change in temperature we are better able to determine the star's pulsation properties from the EUV observations. The star has a EUV magnitude variation with an amplitude of 0.1 mag, and the errors on the magnitude are about 20% of the total amplitude. This is a significant improvement over variations determined from UV studies, and again this is because we are observing farther out on the Wien side of the spectrum. Another aspect of β CMa that has been revealed by our EUV observations is the presence of the beat phenomenon, first discovered in the 1930s in optical studies of β CMa. We will be making further *EUVE* observations at phases of maximal and minimal phase interference to better understand the process as it affects the atmosphere of the star.

The temperature variability seen in the spectrum of β CMa is *consistent* with the β Cephei pulsations seen at other wavelengths, but at least in part this consistency is due to the large error bars on the UV and visual wavelength analyses. We presume that it is possible to better determine the variability of the amplitude in the visual region by using higher sensitivity instruments now available. We strongly encourage such studies. Detailed studies, for example with the *ISO* satellite, will also be required to address the question of atmospheric heating by pulsational/mechanical energy deposition in the outer atmosphere of B stars. We have speculated that the damping of pulsational wave energy might play a role in heating of the outer atmosphere in both ε CMa and β CMa, because the two stars lie just outside and just inside the red edge of the β Cephei strip, respectively.

We are grateful to Mark Abbott of the staff of the Center for EUV Astrophysics for his advice and help in analyzing the data. We benefited from conversations with Steven Kawaler, John Castor, Ronald Reynolds, Ken Nordsieck, Keivan Stassun, Myron Smith, and John Mathis. Jay Holberg's help, with obtaining and processing *Voyager* data, is very much appreciated. We also thank Chris Johns and Keivan Stassun for allowing us to use their Fourier analysis programs. The line identification software was made available to us by Don Lindler. The observations were made as part of the *EUVE* guest observer program, and were funded by NASA grant NAG 5-2282 to the University of Wisconsin and to Eureka Scientific.

REFERENCES

Abbott, D. C. 1982, ApJ, 259, 282
Beeckmans, F., & Burger, M. 1977, A&A, 61, 815
Bouchet, P., Manfroid, J., & Schmider, F. X. 1991, A&AS, 91, 409
Bowen, G. H., & Willson, L. A. 1991, ApJ, 375, L53
Bowyer, S., & Malina, R. F. 1991, in Extreme Ultraviolet Astronomy, ed. R. F. Malina, & S. Bowyer (New York: Pergamon), 397
Cassinelli, J. P., et al. 1995, ApJ, 438, 932 (Paper I)
Cheng, K.-P., & Bruhweiler, F. C. 1990, ApJ, 335, 188
Code, A. D., Davis, J., Bless, R. C., & Hanbury Brown, R. 1976, ApJ, 203, 417
Code, A. D., & Meade, M. R. 1979, ApJS, 39, 195
Cohen, M., Walker, R. G., Barlow, M. J., & Deacon, J. R. 1992, AJ, 104, 1650
Drew, J. E., Denby, M., & Hoare, M. G. 1994, MNRAS, 266, 917
Dupuis, J., et al. 1995, ApJ, submitted
Frisch, P. 1994, Science, 265, 1423
Gry, C., York, D. G., & Vidal-Madjar A. 1985, ApJ, 296, 593
Gry, C. 1995, private communication
Hanbury Brown, R., Davis, J., & Allen, L. R. 1974, MNRAS, 167, 121
Hayes, D. S. 1985, in IAU Symp. 111, Calibration of Fundamental Stellar Quantities, ed. D. S. Hayes, L. E. Pasinetti, & A. G. Davis Philip (Dordrecht: Reidel), 225

Hoare, M. G., Drew, J. E., & Denby, M. 1993, MNRAS, 262, L19
Hubeny, I. 1988, Comp. Phys. Comm., 52, 103
Hubeny, I., & Lanz, T. 1992, A&A, 262, 501
———. 1995a, in IAU Colloq. 152, Astrophysics in the Extreme Ultraviolet, in press
———. 1995b, 439, 875
Hoffliet, D., & Jaschek, C. 1982, Bright Star Catalog (New Haven: Yale Univ. Press).
IRAS Point Source Catalog. 1988, IRAS Catalogues and Atlases (NASA RP-1190)
Iglesias, C. A., & Rogers, F. J. 1991, ApJ, 371, 408
Jamar, C., Macau-Hercot, D., Monfils, A., Thompson, G. I., Houziaux, L., & Wilson, R. 1976, Ultraviolet Bright Star Photometric Catalogue (ESA SR-27)
Johnson, H. L., & Mitchell, R. I. 1975, Rev. Mexicana Astron. Af., 1, 3
Johnson, H. L., Mitchell, R. I., Iriarte, B., & Wiśniewski, W. Z. 1966, Comm. Lunar Planetary Lab., 4, 99
Kiriakidis, M., El Eid, M. F., & Glatzel, W. 1992, MNRAS, 255, 1P
Kudritzki, R. P., Pauldrach, A., Puls, J., & Abbott, D. C. 1989, A&A, 219, 205
Kurucz, R. L. 1992, in IAU Symp 149, *The Stellar Populations of Galaxies*, ed. B. Barbury & A. Renzini (Dordrecht: Kluwer), 225
Kutyrev, A., & Reynolds, R. 1995, private communication
Lamers, H. J. G. L. M., Cerruti-Sola, M., & Perinotto, M. 1987, ApJ, 314, 726
Lampton, M., Margon, B., & Bowyer, S. 1976, ApJ, 208, 177
Linsky, J. L. Brown, A., Gayley, K., Diplas, A., Savage, B. D., Ayres, T. R., Landsman, W., Shore, S. N., & Heap, S. R., 1993, ApJ, 402, 694
MacFarlane, J. J., Cohen, D. H., & Wang, P. 1994, ApJ, 437, 351
MacFarlane, J. J., Cohen, D. H., Cassinelli, J. P., & Wang, P. 1995, in IAU Colloq. 152, Astrophysics in the Extreme Ultraviolet, in press
Meyer, W. F. 1934, PASP, 46, 202
Moskalik, P., & Dziembowski, W. 1992, A&A, 256, L5
Najarro, F., Kudritzki, R. P., Cassinelli, J. P., Stahl, O., & Hillier, D. J. 1995, A&A, in press
Perry, C. L., Olsen, E. H., & Crawford, D. L., 1987, PASP, 99, 1184
Remie, H., & Lamers, H. J. G. L. M. 1982, A&A, 105, 85
Shobbrook, R. R. 1973, MNRAS, 101, 257
Sterken, C., & Jerzykiewicz, M. 1993, Space Sci. Rev., 62, 95
Uisugi, A., & Fukuda, I. 1982, Revised Catalog of Stellar Rotational Velocities (Kyoto: Kyoto Univ.)
Vallerga, J. V., Siegmund, O. H. W., Vedder, P. W., & Gibson, J. L. 1991, Nucl. Instr. Methods, 310, 317
Vennes, S., Dupuis, J., Bowyer, S., Fontaine, G., Wiercigroch, A., Jelinsky, P., Wesemael, F., & Malina, R. 1993, ApJ, 421, L35
Vidal, C. R., Cooper, J., & Smith, E. W. 1973, ApJS, 25, 37
Watson, R. D. 1972, ApJS, 24, 167
Welsh, B. Y. 1991, ApJ, 373, 556